Korean J. Chem. Eng., 40(5), 1197-1208 (2023)
DOI: 10.1007/s11814-022-1338-2

pISSN: 0256-1115
eISSN: 1975-7220

Effects of surface silylation on dye removal performance of mesoporous promoted titania-silica nanocomposite

Parham Haghighi*, Amin Bazyari*,†, Somayeh Alijani, Fatemeh Khademian*, and Levi Theodore Thompson***,†**

*Catalysis and Nanomaterials Research Laboratory, School of Chemical, Petroleum, and Gas Engineering, Iran University of Science and Technology, P. O. Box 16765-163, Tehran, Iran
**Energy and Environment Research Center, Niroo Research Institute, P. O. Box 14665-517, Tehran, Iran
***Department of Chemical and Biomolecular Engineering, University of Delaware, Newark, DE, 19717 USA
(*Received 2 July 2022 • Revised 6 October 2022 • Accepted 6 November 2022*)

Abstract−Surface modification of a mesoporous tungsten- and bismuth-promoted titania-silica nanocomposite was conducted by a silylation method using hexamethyldisilazane (HMDS) as the silylation reagent to overcome the low adsorption capacity of TiO_2-based photocatalysts for organic dyes, which subsequently enhances photodegradation of the organic dyes under visible light irradiation. The performance of the nanocomposites was evaluated by photodegradation of Rhodamine B (RhB) dye under visible light irradiation in a triple-walled immersion well reactor. The synthesized nanocomposites were characterized by N_2 adsorption-desorption, FE-SEM, XRD, SAED pattern, HR-TEM, EDX, FTIR, UV-Vis DRS, PL spectroscopy, TGA, and water contact angle measurement to determine the bulk structure and surface properties before and after surface silylation. The results revealed that surface hydroxyl groups were successfully replaced by the silyl groups via the silylation process, without significant alterations in the structure and textural properties of the nanocomposite. In addition, silylation of the nanocomposite surface significantly enhanced the adsorption capacity of RhB molecules due to increased surface hydrophobicity, which accelerated the photocatalytic degradation of RhB in water. The results of the photocatalytic degradation experiments demonstrated that although all the synthesized nanocomposites were able to remove all RhB molecules from water after 240 minutes of the reaction, the optimized silylated sample with 0.15 g of HMDS (TSWBi-Sil3) was able to remove 92% of the RhB after only 90 minutes, while it was only 79% for the unmodified nanocomposite.

Keywords: Silylation, Nanocomposite, Titania-silica, Photocatalyst, Rhodamine B

INTRODUCTION

Industrial development has led to the discharge of various types of toxic pollutants, such as organic substances into the water sources, which threatens the ecosystem and public health and causes significant problems such as environmental contamination, reduction of drinking water resources, and so on [1-5]. Among water pollutants, organic dyes in the effluents of industries are the main reasons for water pollution because they are highly hazardous, carcinogenic, and non-biodegradable. Even a low concentration of organic dyes (<1 ppm) is clearly visible in water and adversely impacts the aquatic environment. Therefore, removing organic dyes from wastewater streams is of great scientific and industrial significance [6-14].

Unfortunately, conventional water treatment methods such as adsorption, coagulation and flocculation, and filtration, are not effective enough, because they require long-term and expensive operations and produce secondary pollutants [7,15,16]. On the other hand, advanced oxidation processes (AOPs) are effective for degrading a wide range of dyes using hydroxyl and superoxide radicals. Among various AOPs, the TiO_2-based environmentally benign photocatalytic process appears to be one of the most effective techniques to mineralize organic dyes and produce harmless by-products (e.g., H_2O and CO_2) at the ambient temperature and pressure [17-20]. Some limitations and challenges, including inefficient utilization of visible light due to large band gap, low adsorption capability, and fast electron-hole (e^--h^+) recombination, have prevented the full-scale application of the TiO_2 photocatalyst [17-19,21-25]. Therefore, various bulk and surface modification methods have been utilized to improve the photocatalytic activity of TiO_2. Recent studies have shown that promoting TiO_2 with Bi or W oxides increased photocatalytic activity under visible light irradiation, which is related to higher visible light absorption and improved charge separation [26-33].

Note that organic dyes must be pre-adsorbed on the surface of the photocatalyst to be photodegraded efficiently [34,35]. The low adsorption capacity of TiO_2 for organic dyes arises from its surface chemistry, which is dominated by hydrophilic hydroxyl functional groups [23]. Organic dye pollutants are usually hydrophobic, and therefore the hydrophilic/hydrophobic properties of the TiO_2 surface play an essential role in their adsorption and subsequent degradation [36]. One of the surface modification techniques to increase the surface hydrophobicity and adsorption capacity of the oxide materials is silylation, which means partial replacement of the terminal hydroxyl groups by silyl (R_3Si) groups. Yan et al. [37] synthesized surface-modified TiO_2 nanotube arrays (TiO_2-NT) using silane coupling agent KH570 to degrade organic pollutants. The results

†To whom correspondence should be addressed.
E-mail: abazyari@iust.ac.ir, ltt@udel.edu

indicated that the surface modification enhanced the adsorption of hydrophobic organic compounds, leading to improved dye degradation. Therefore, silylation may be considered an effective strategy to augment the adsorptive-photocatalytic performance of oxide photocatalysts.

In addition to using Bi and W oxides promoters and surface silylation, results have shown that accelerated adsorption of organic molecules and their subsequent photocatalytic degradation may be achieved if the TiO_2 active phase is supported on high surface area and mesoporous adsorbents such as silica, zeolites, activated carbon, and polymers [38-42]. The high-surface-area support provides highly dispersed titanium species or TiO_2 nanoparticles, resulting in enhanced photocatalytic efficiency. At the same time, mesoporous structure facilitates the diffusion of bulky dye molecules into the photocatalyst pores where most of the active sites are located. Kuwahara et al. [38,39,43] synthesized silylated zeolite and mesoporous silica using triethoxyfluorosilane (TEFS), used them as support for TiO_2, and investigated the effects of the support silylation on the photodegradation of 2-propanol, acetaldehyde, and phenol. They reported an enhanced crystal growth of TiO_2 nanoparticles in the mesopores and increased thermal stability and surface area as the advantages of exploitation of the mesoporous silica supports. Additionally, it was found that silylation caused greater adsorption of organic pollutants as compared to H_2O molecules. In another study, Ohno et al. [44] prepared TiO_2-SiO_2 composites modified with alkylsilyl groups and evaluated their photoactivity for oxidation of aldehyde compounds in aqueous media. Results demonstrated enhanced adsorption and photo-oxidation of aldehydes due to the interaction among the functional groups introduced on the SiO_2-TiO_2 surface and the hydrocarbon molecules.

Therefore, the principal objective of the present study was to synthesize a silylated tungsten- and bismuth-promoted titania-silica mixed oxide material and use it as a photocatalyst-adsorbent for photocatalytic degradation of a bulky organic dye as RhB. The TiO_2 active phase was first dispersed on SiO_2 support and modified with tungsten and bismuth oxides to increase its visible light photocatalytic performance. Then, silylation of tungsten- and bismuth-promoted titania-silica was used to increase its hydrophobicity and adsorption capability for organic pollutants. It was hypothesized that co-utilization of SiO_2 support, Bi and W oxides promoters, and surface silylation might synergistically help overcome the two above-mentioned limitations of TiO_2-based photocatalysts. To the best of our knowledge, there is no report on the visible light degradation of organic dyes over silylated nanostructured tungsten- and bismuth-promoted titania-silica mixed oxide photocatalyst-adsorbent as opposed to several studies published on the materials with single modifications. This may pave the way for development of high-performance photocatalysts with the chance for large-scale applications.

EXPERIMENTAL

1. Chemicals

All chemicals were used as received without further purification. High-purity silica (SiO_2, ≥99.9%) was purchased from Aldrich. Ethanol (≥99.9%), tetra-*n*-butyl orthotitanate (TBOT, ≥98.5%), sodium tungstate dihydrate ($Na_2WO_4{\cdot}2H_2O$, ≥99%), bismuth (III) nitrate pentahydrate ($Bi(NO_3)_3{\cdot}5H_2O$, ≥98%), toluene (≥99%), and Rhodamine B (RhB, ≥95%) were all obtained from Merck. Hexamethyldisilazane (HMDS, ≥99.5%) was purchased from Fluka.

2. Synthesis of SiO_2-supported TiO_2 Photocatalyst

The TiO_2-SiO_2 nanocomposite with TiO_2 loading of 50 wt% was synthesized using the conventional wet impregnation method, as the procedure reported in [38] with some alterations. Typically, the SiO_2 (1.0 g) was suspended in a mixed solution of TBOT (2.13 g) and ethanol (15 g) and then stirred at room temperature for 3 h. Next, the mixture was stirred at 80 °C for an additional 2 h, followed by drying at 110 °C overnight and calcination for 5 h at 500 °C. The as-prepared material was labeled as TS.

3. Synthesis of W- and Bi-promoted TiO_2-SiO_2 Photocatalyst

The nanostructured W- and Bi-promoted TiO_2/SiO_2 mixed oxide with 1 wt% W and Bi loading was synthesized using the wet impregnation method based on the procedure reported elsewhere [45,46]. Based on earlier experimental results in our study group, a 1 wt% loading of W and Bi was chosen. Generally, TiO_2/SiO_2 (1.0 g) was suspended in 50 mL deionized water, stirred for 30 min, and then sonicated employing an ultrasonic cleaner for 30 min. Later, the mixed solutions of $Na_2WO_4{\cdot}2H_2O$ (0.00179 g/mL) and $Bi(NO_3)_3{\cdot}5H_2O$ (0.00232 g/mL) were added into the first mixture and stirred for 3 h at room temperature and an extra 1 h at 70 °C. Finally, the obtained suspension was dried at 90 °C overnight and calcined at 450 °C for 5 h in air. TSWBi was the name given to the prepared sample.

4. Silylation of W- and Bi-promoted TiO_2/SiO_2

The silylation of W- and Bi-promoted TiO_2/SiO_2 involved using the experimental setup shown in Fig. 1, according to the procedure described in [47], with some modifications. First, the material (0.5 g) was dried for 2 h at 120 °C and then suspended in a mixed solution of certain amounts of HMDS and 10 mL of tolu-

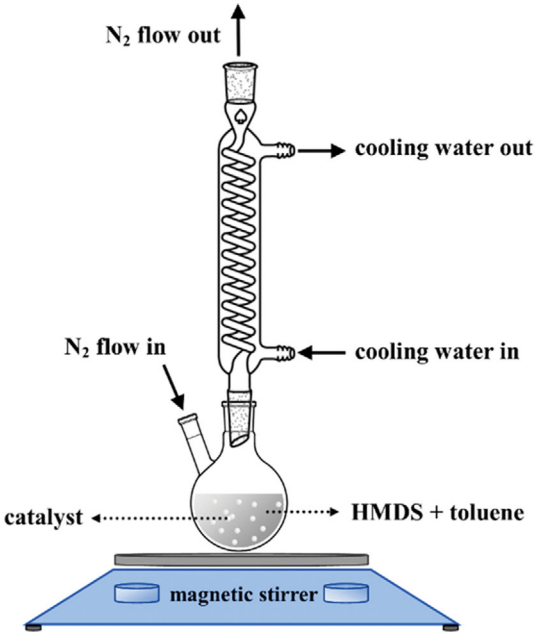

Fig. 1. The experimental setup used for silylation of the materials.

ene. The mixture was stirred under a nitrogen blanket and reflux conditions at room temperature for 12 h. Lastly, the products were filtered, washed with 10 mL toluene, and dried overnight at 120 °C. The surface-modified photocatalysts by 0.03, 0.10, and 0.15 g of HMDS were labeled as TSWBi-Sil1, TSWBi-Sil2, and TSWBi-Sil3, respectively.

5. Characterization of Photocatalysts

X-ray powder diffraction (XRD) was carried out to analyze the crystalline structure of photocatalysts using Bourevestink DRON-8 equipped with Cu-kα X-Ray source in 2θ of range of 5-80°. Textural properties, including surface area, pore size distribution, and pore volume of the samples, were determined using N_2 adsorption-desorption isotherms obtained at 77 K in liquid nitrogen employing Belsorp mini apparatus. The samples were degassed at 100 °C for 4 h under vacuum before N_2 adsorption-desorption measurement. Fourier-transform infrared spectroscopy (FTIR) spectra were recorded on a Thermo AVATAR spectrometer with a resolution of 2 cm^{-1} in the range of 4,000-450 cm^{-1} using KBr disks containing 1% (w/w) of the finely ground powder samples. The surface morphology of the materials was probed using a field emission scanning electron microscope (FE-SEM) on TESCAN MIRA3 instrument operating at 26 kV. Also, the constituting elements of the samples were characterized by energy dispersive X-ray spectroscopy (EDX) on the same instrument. The microstructure and crystallinity of the samples were investigated by means of high resolution transmission electron microscopy (HR-TEM) and selected area electron diffraction (SAED) on an FEI Tecnai G2 F20 with an acceleration voltage of 200 kV. The optical properties and behavior of light-induced charge carriers of the photocatalysts were investigated employing UV-vis spectrophotometry (Shimadzu UV-2550 Spectrometer) and the photoluminescence (Perkin-Elmer LS-55 fluorescence spectrometer), respectively. The thermal decomposition behavior of the prepared photocatalysts was investigated by thermogravimetry analysis (TGA) performed on an STA504 analyzer under Argon flow in the temperature range of 50-1,000 °C. Calculating the contact angle of a pure water droplet on the surface of the pelletized photocatalyst was utilized to determine the hydrophobicity of the samples using a DINOLITE digital optical microscope.

6. Evaluation of Photocatalytic Activities

The photocatalytic activity of the synthesized photocatalysts was evaluated by the photodegradation of RhB (10 mg/L) under visible light irradiation. 0.10 g of photocatalyst and 100 mL of aqueous RhB solution were placed into a triple-walled quartz immersion well photoreactor equipped with a 150 W tungsten halogen lamp as the visible light source (Fig. 2). The dye solution was cooled to room temperature by circulating tap water through a surrounding quartz jacket. Moreover, the photocatalytic tests were carried out under ambient air-equilibrated conditions. The solution was stirred for 1 h under dark conditions to obtain adsorption-desorption equilibrium, followed by visible light illumination for a further 3 h while stirring. The percentage of dye removal was measured by taking samples (3 mL) from the photoreactor at intervals of 30 minutes. The samples were centrifuged and analyzed quantitatively by a Shimadzu UV-2401PC UV-vis spectrophotometer.

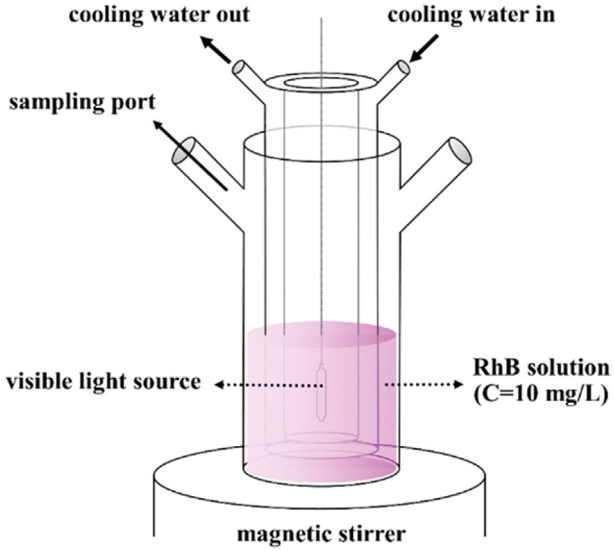

Fig. 2. The triple-walled quartz immersion well photoreactor for RhB degradation.

RESULTS AND DISCUSSION

1. Characterization of Photocatalysts

The reaction of HMDS on the surface of the photocatalyst is shown in Scheme 1. As implied, the silylation reaction involves replacing the surface hydroxyl groups of TiO_2 and SiO_2 with the silyl groups. The surface properties and structure of the prepared samples were characterized by N_2 adsorption-desorption, FE-SEM, XRD, SAED pattern, HR-TEM, EDX, FTIR, UV-Vis DRS, PL, and water contact angle measurements. The detailed results are discussed as follows.

1-1. N_2 Adsorption-desorption

The textural properties of TiO_2, TS, TSWBi, and the optimized

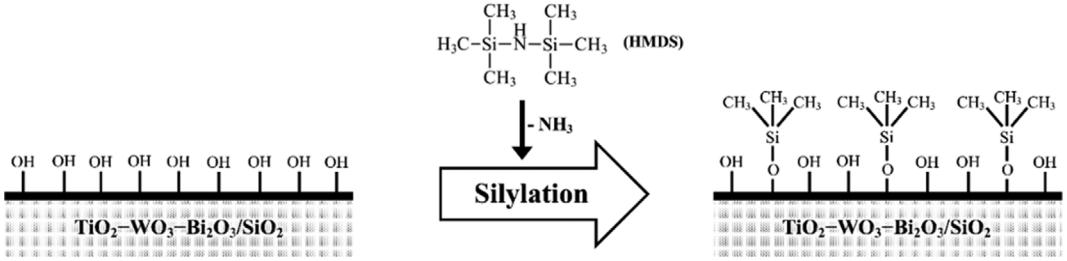

Scheme 1. Schematic diagram of the silylation reaction of HMDS on the surface of W- and Bi-promoted TiO_2/SiO_2 mixed oxide photocatalyst-adsorbent.

Table 1. Textural properties of synthesized photocatalysts

Sample	BET surface area (m^2/g)	Pore volume (cm^3/g)	Average pore diameter (nm)	Crystallite size (nm)
TiO_2	0.2	0.01	44	26.6
TS	122	0.32	10.5	8.8
TSWBi	156	0.26	9.0	8.9
TSWBi-Sil3	135	0.23	8.3	9.0

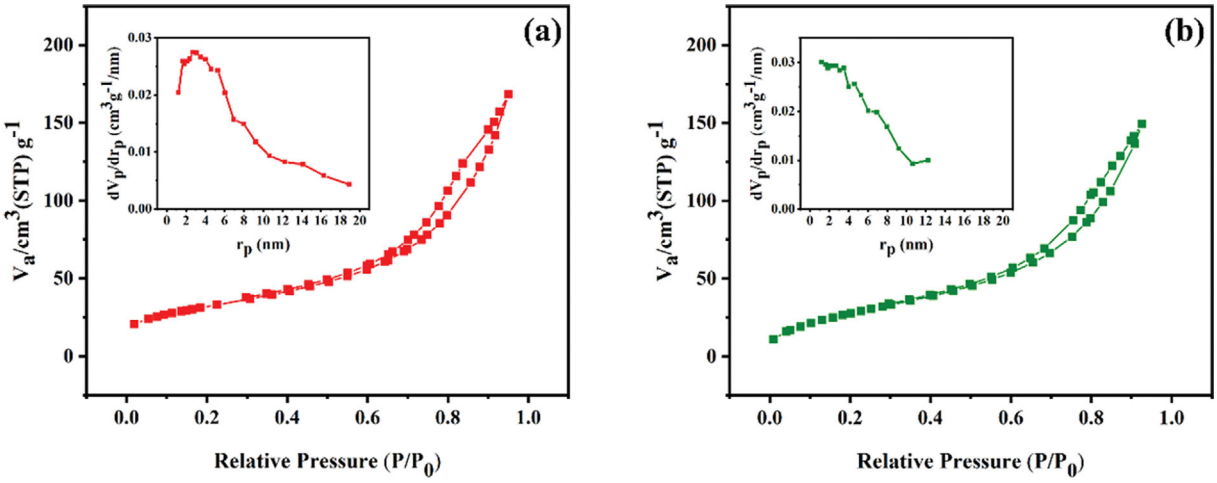

Fig. 3. N_2 adsorption-desorption isotherms and BJH pore size distributions of (a) TSWBi and (b) TSWBi-Sil3.

silylated photocatalyst, i.e., TSWBi-Sil3, are summarized in Table 1. The N_2 adsorption-desorption isotherms and the BJH pore size distributions of TSWBi and TSWBi-Sil3 are shown Fig. 3. The existence of SiO_2 support in TS compared to pure TiO_2 can cause the catalyst surface area and pore volume to increase. Fabrication of such mixed oxide photocatalysts with a large surface area and mesoporous structure is beneficial for effective pollution absorption and subsequent degradation. The TSWBi sample exhibited higher surface area and slightly lower pore diameter and average pore volume than TS, suggesting clogging of some micropores and uniform distribution of the bismuth and tungsten species on the TS pore walls. In addition, all textural properties decreased slightly after silylation, most likely due to the replacement of small surface hydroxyl groups with larger silyl groups. This may not induce significant changes in the diffusion of RhB molecules into the pores of TSWBi-Sil3, as reported in the literature [48,49]. The TSWBi and TSWBi-Sil3 samples exhibited type-IV isotherms with H1 hysteresis loops, which according to the IUPAC classification, are traits of mesoporous materials. This implies that the mesoporous structure of the photocatalyst did not change considerably after surface modification by HMDS.

1-2. X-ray Diffraction (XRD)

The X-ray diffraction patterns were used to investigate the effects of silylation modification on the crystallinity of TSWBi photocatalyst. As can be seen from Fig. 4, the XRD diffractograms were almost identical for TSWBi sample and silylated photocatalysts, indicating that surface silylation by HMDS did not change the crystalline structure of TSWBi. Therefore, any side effects of the silylation treatment on the photocatalytic performance due to crystallinity change

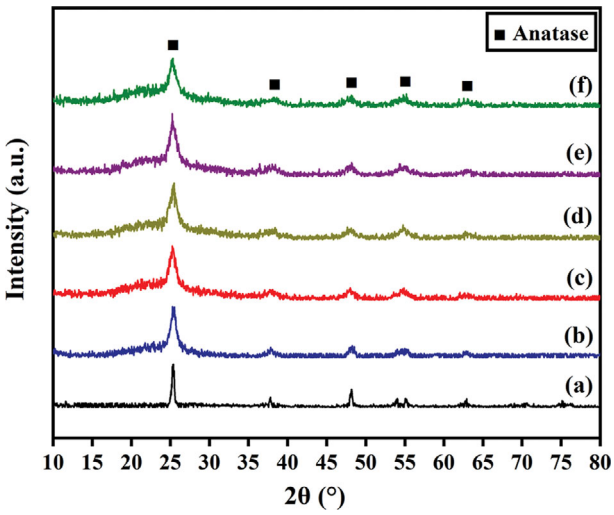

Fig. 4. XRD patterns of (a) TiO_2, (b) TS, (c) TSWBi, (d) TSWBi-Sil1, (e) TSWBi-Sil2, and (f) TSWBi-Sil3.

could be excluded. Moreover, anatase TiO_2 was the only crystalline phase observed, and no diffraction peak for the SiO_2 was identified, implying an amorphous structure of SiO_2. The SiO_2 support may enhance the stability of the anatase TiO_2 during calcination or high-temperature regeneration process and was able to successfully impede the growth of anatase crystallites and prevent the formation of less active rutile phase. The crystallite size, calculated by the Scherrer formula employing the broadening of the anatase TiO_2

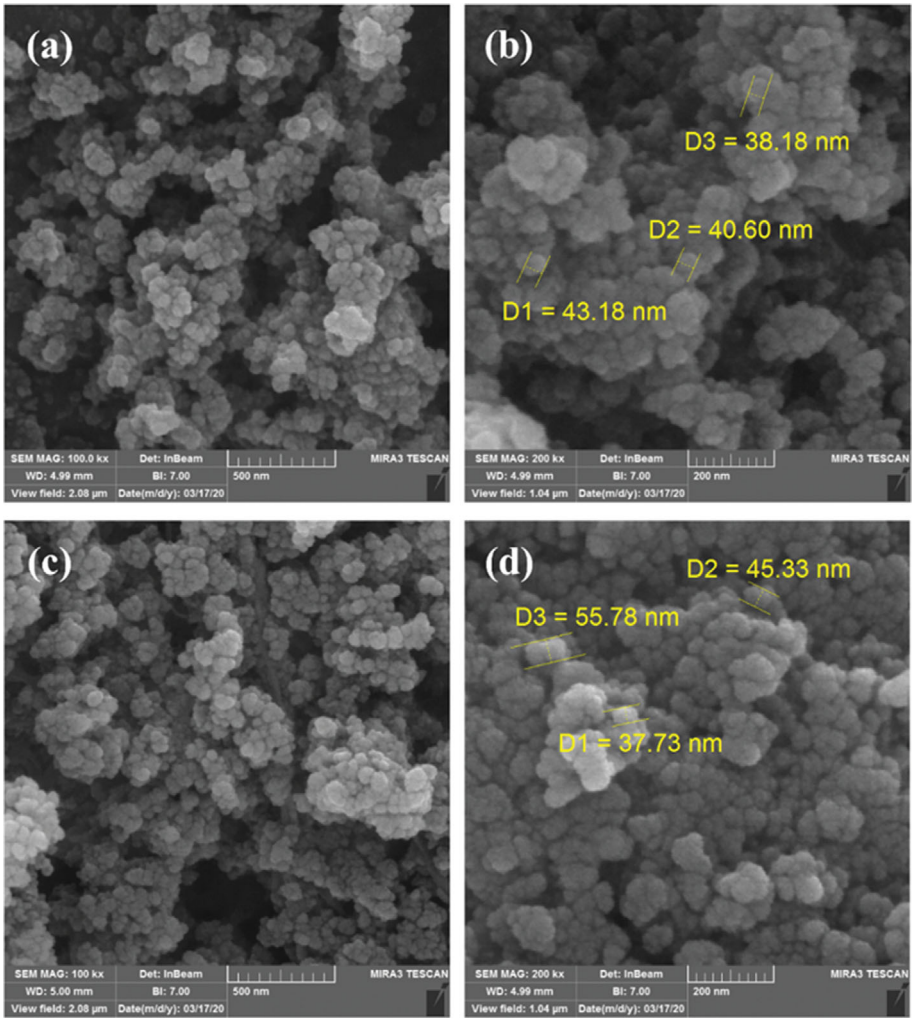

Fig. 5. FE-SEM images of (a), (b) TSWBi and (c), (d) TSWBi-Sil3.

(101) reflection peak, remained constant at ~9.0 nm (see Table 1). Note that there were no observable diffraction peaks for the tungsten or bismuth oxides. This was expected because the promoter concentrations (1.0 wt%) were below the XRD detection limit [33].

1-3. Field Emission Scanning Electron Microscopy (FE-SEM) and Energy Dispersive X-ray (EDX)

The FE-SEM images shown in Fig. 5 clearly confirm that surface silylation did not change the morphology and mean particle size of the optimized TSWBi photocatalyst. The EDX spectra revealed Si, Ti, and O as the constituting elements of the TS photocatalyst without any impurities, as shown in Fig. 6. After W and Bi loading, these elements were added to the rest of the ingredients. In addition, the EDX spectrum of the silylated photocatalysts (TSWBi-Sil1, TSWBi-Sil2, and TSWBi-Sil3), shown in Fig. 6, confirmed the existence of carbon in addition to other elements (Si, Ti, W, and Bi) observed for the TSWBi. This can be ascribed to the successful loading of silyl groups on the surface of the modified photocatalyst.

1-4. High Resolution Transmission Electron Microscopy (HR-TEM) and Selected Area Electron Diffraction (SAED) Pattern

Fig. 7 shows the representative HR-TEM and SAED images of the optimized silylated photocatalyst (TSWBi-Sil3). It can be seen from Fig. 7(a) that TSWBi-Sil3 is a composite of crystalline anatase and amorphous silica. As shown in Fig. 7(b), the lattice spacing in the sample was found to be almost 0.35 nm, which corresponds to the (101) plane of anatase TiO_2 [50,51]. This further indicates suppression of rutile formation. To further reveal the crystalline nature, SAED was also carried out on the TSWBi-sil3 photocatalyst, as shown in Fig. 7(c). The bright diffraction rings may be ascribed to (101), (004), (200), (211), and (204) planes of anatase TiO_2, which are in good agreement with XRD findings [52].

1-5. Fourier-transform Infrared (FTIR) Spectroscopy

The FTIR spectra of photocatalysts before and after silylation in the range of 450-4,000 cm^{-1} are presented in Fig. 8. As seen, the characteristic peaks were detected at 795, 952, 1,100, 1,633, 2,926, and 3,433 cm^{-1}. The peaks centered at 795 cm^{-1} and 1,100 cm^{-1} are ascribed to symmetric and asymmetric stretching vibrations of Si-O-Si bond, respectively [52]. Besides, the peak observed at ~952 cm^{-1} can be assigned to Si-O-Ti stretching vibration [53]. No discernible signal attributable to Bi and W linkages could be detected due to low concentrations of these elements. The peak at 1,633 cm^{-1} is attributable to the bending vibration of the adsorbed water molecules due to the hydrophilic properties of surface hydroxyl

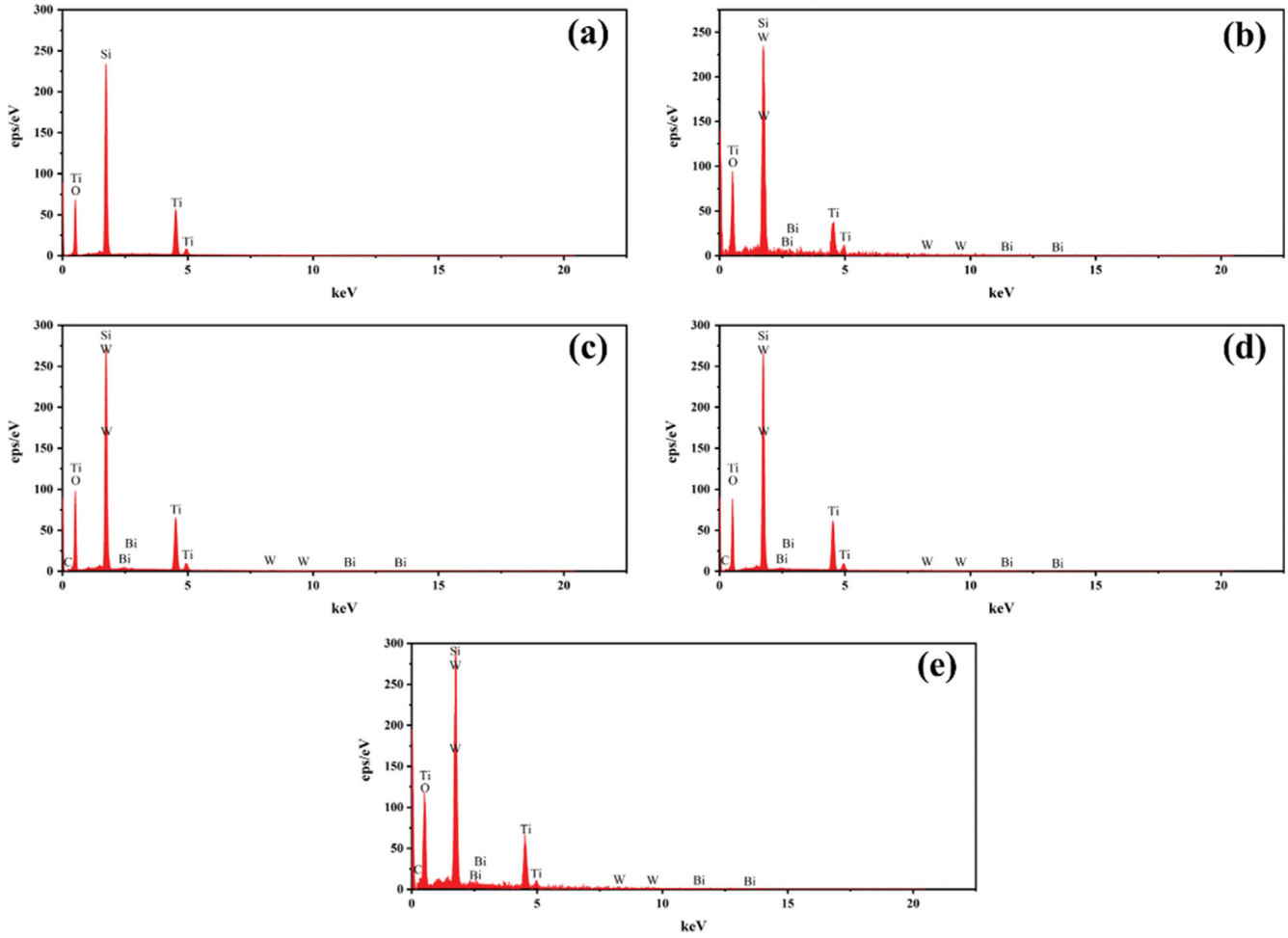

Fig. 6. EDX spectra of (a) TS, (b) TSWBi, (c) TSWBi-Sil1, (d) TSWBi-Sil2, and (e) TSWBi-Sil3.

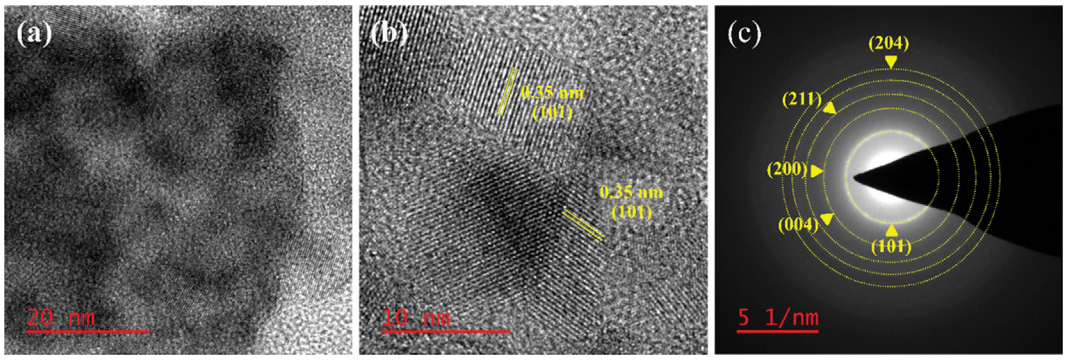

Fig. 7. (a), (b) HR-TEM images, and (c) SAED pattern of TSWBi-Sil3.

groups. Furthermore, the strong broad peak centered at 3,433 cm^{-1} is ascribed to O-H stretching vibration caused by the adsorbed water molecules and surface hydroxyl groups [49,54]. Results revealed that the intensity of these peaks was significantly decreased in the silylated sample. Therefore, surface hydrophobicity was improved by replacing the surface hydroxyl groups with the silyl groups of HMDS. Moreover, a peak with lower intensity at 2,900 cm^{-1} was only observed in the silylated photocatalyst, which may be assigned to the vibration of C-H bonds arising from methyl groups (-CH_3) on the surface [54]. Accordingly, the silylation treatment is expected to enhance the photodegradation of organic dyes by reducing the water molecules accumulation on the surface of the silylated sample.

1-6. Photoluminescence (PL) Spectroscopy

The room-temperature PL spectra of the synthesized photocatalysts were measured at an excitation wavelength of 300 nm to investigate the migration, transfer, and recombination properties of the photo induced electron/hole pairs. As seen in Fig. 9, the addition of bismuth and tungsten oxides significantly decreased the intensity of

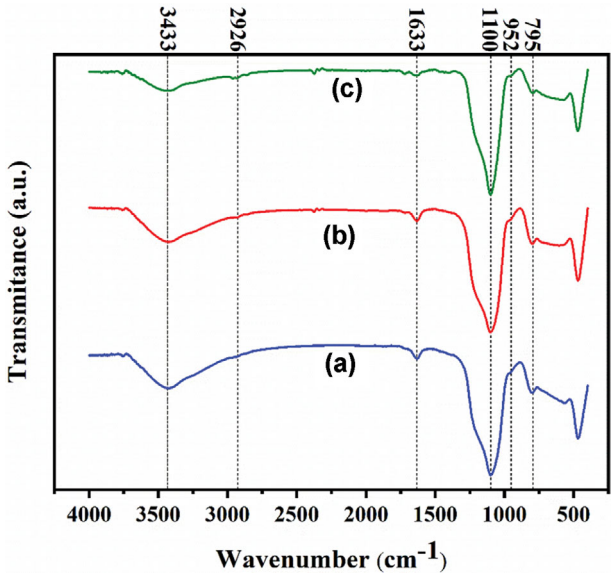

Fig. 8. FTIR spectra of (a) TS, (b) TSWBi, and (c) TSWBi-Sil3.

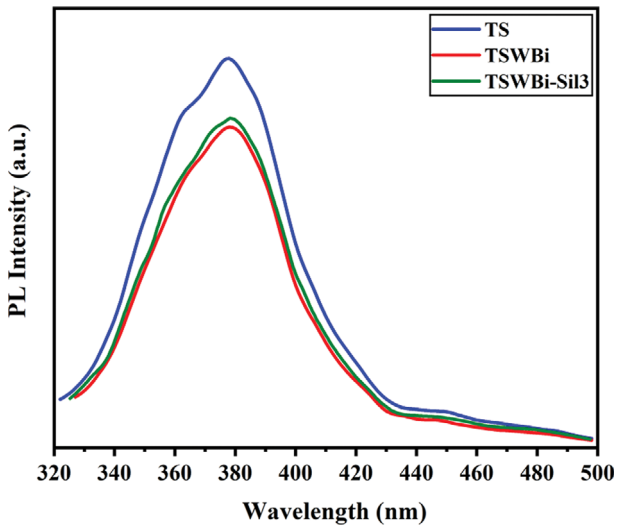

Fig. 9. PL spectra of the TS, TSWBi, and TSWBi-Sil3 photocatalysts.

the PL spectra. It is well documented that a lower PL peak intensity originates from a lower recombination rate, which may increase photocatalytic degradation efficiency under visible light irradiation [55]. In addition, it was confirmed that surface silylation did not significantly alter the PL peak intensity and charge carriers properties.

1-7. UV-vis Diffuse Reflectance Spectroscopy (DRS)

The optical absorption behavior of the TS, TSWBi, and TSWBi-Sil3 samples was evaluated employing UV-vis DRS (see Fig. 10(a)). A slight red shift was observed upon adding bismuth and tungsten oxides compared to TS photocatalyst. Also, it was found that the silylation process did not change the optical absorption edge of the photocatalyst. Fig. 10(b) indicates the Tauc plot $((\alpha h\nu)^{1/2}$ versus $h\nu$) to estimate the band gap energy (Eg) of the photocatalysts. The estimated Eg value using Kubelka-Munk function for the TS, TSWBi, and TSWBi-Sil3 photocatalysts was 3.18, 3.05, and 3.06 eV, respectively. Thus, it can be expected that the TSWBi and TSWBi-Sil3 samples show a superior photodegradation performance under the visible range compared to TS sample.

1-8. Thermogravimetry Analysis (TGA)

To evaluate the thermal stability of photocatalysts and examine the effect of surface silylation, TGA was employed, as shown in Fig. 11. Weakly adsorbed water is removed from the surface at temperatures lower than 120 °C. More strongly adsorbed water is removed between 120 °C and 300 °C [47]. As clearly seen, the silylated photocatalyst (TSWBi-Sil3) underwent much lower weight losses than the unmodified sample (TSWBi) in these temperatures due to greater hydrophobicity. The weight loss of the TSWBi was found to be nearly 32.3%, while it was only 8.5% for the TSWBi-Sil3. In addition, the weight loss of TSWBi-Sil3 at temperatures more than 400 °C is ascribed to the decomposition of methyl groups on the surface [49].

1-9. Water Contact Angle Measurement

Water contact angle measurements were conducted on the silylated TSWBi-Sil3 and unmodified TSWBi samples to evaluate the hydrophobicity of the synthesized materials. As is shown in Fig. 12,

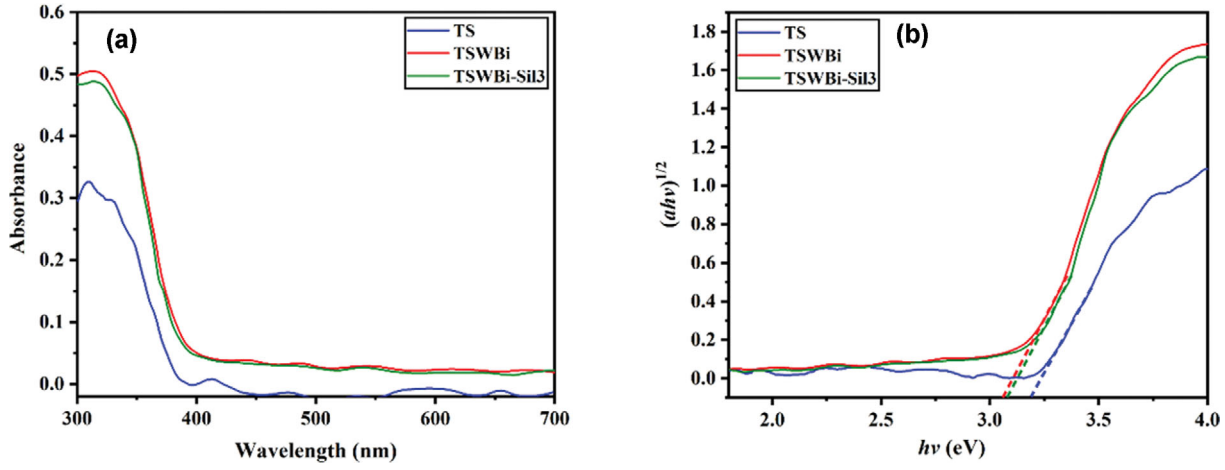

Fig. 10. (a) UV-vis DRS spectra and (b) the plots of $(\alpha h\nu)^{1/2}$ versus $h\nu$ for TS, TSWBi, and TSWBi-Sil3 photocatalysts.

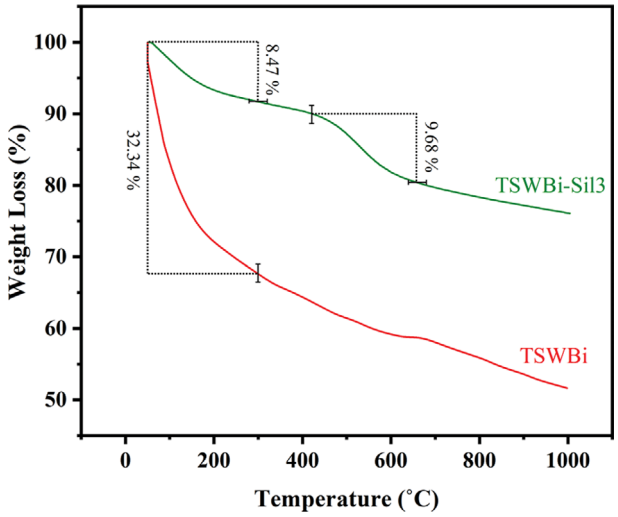

Fig. 11. TG profiles of unmodified and silylated photocatalysts.

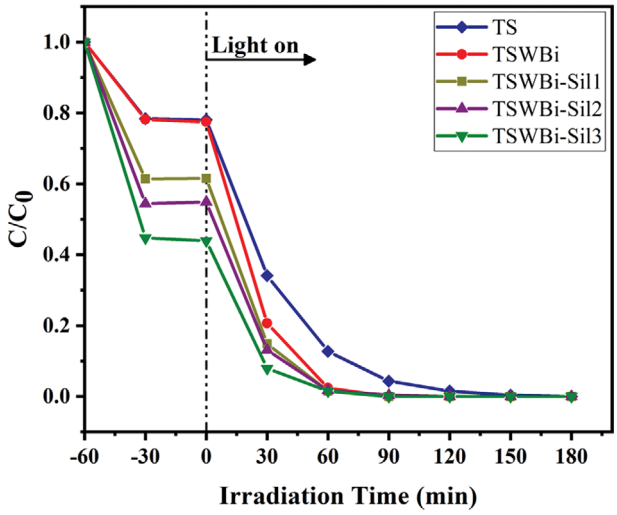

Fig. 13. Photocatalytic degradation of RhB by different photocatalyst-adsorbents (T=25 °C, P=1 atm, C_0=10 mg/L, photocatalyst dose=1 g/L).

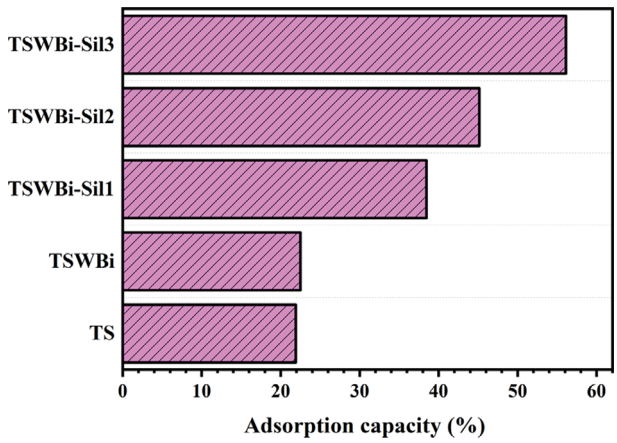

Fig. 14. Adsorption capacity of different photocatalyst-adsorbents for RhB in dark condition.

the contact angle of the water droplet on the TSWBi-Sil3 pellet was much larger (122°) than that on TSWBi pellet, indicating the improvement of surface hydrophobicity due to silylation process. The hydroxyl groups were replaced by Si-$(CH_3)_3$ groups (see Scheme 1) on the surface of TSWBi-Sil3, which was verified by FTIR analysis. According to reports, the tendency of hydrophobic photocatalysts toward the adsorption of organic pollutants is higher compared to the hydrophilic counterparts, which results in improved photocatalytic efficiency [56]. It is noticed that the degree of photocatalyst dispersion in an aqueous dye solution changes depending on the hydrophobic/hydrophilic properties of the materials. Thus, it is necessary to use an optimum amount of silylation to prevent extensive segregation of the silylated photocatalyst, reducing the efficient contact between the catalyst and the solution.

1-10. Measurement of Visible Light Photoactivity

The effects of Bi and W promoters as well as surface silylation on the SiO_2-supported TiO_2 photocatalyst were investigated by the photodegradation of RhB diluted in water (10 mg/L) under visible light irradiation. Fig. 13 shows the reaction time profiles for the removal of RhB using the synthesized photocatalyst-adsorbents. Each test was performed for 1 h in the dark condition to reach the adsorption-desorption equilibrium, followed by visible light irradiation for an additional 3 h. As is seen, the adsorption of RhB molecules was completed during the first 30 min. All silylated materials exhibited higher adsorption capacity compared to the TS (22%) and TSWBi (23%) photocatalysts (Fig. 14). The displacement of hydroxyl group by the silyl group occurs on the surface of silylated TSWBi,

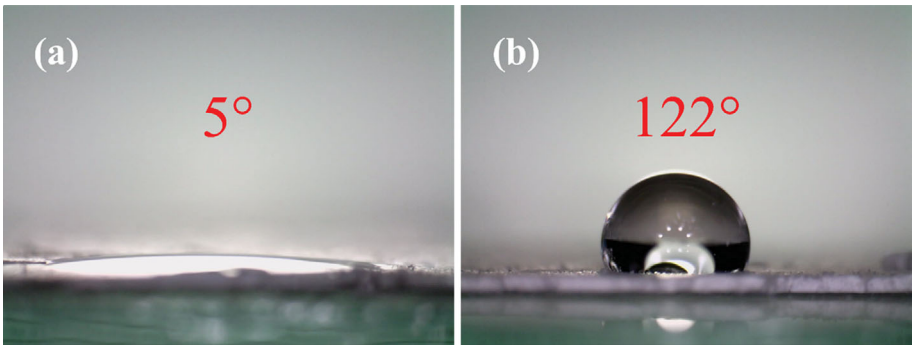

Fig. 12. Water contact angle measurements of (a) TSWBi and (b) TSWBi-Sil3.

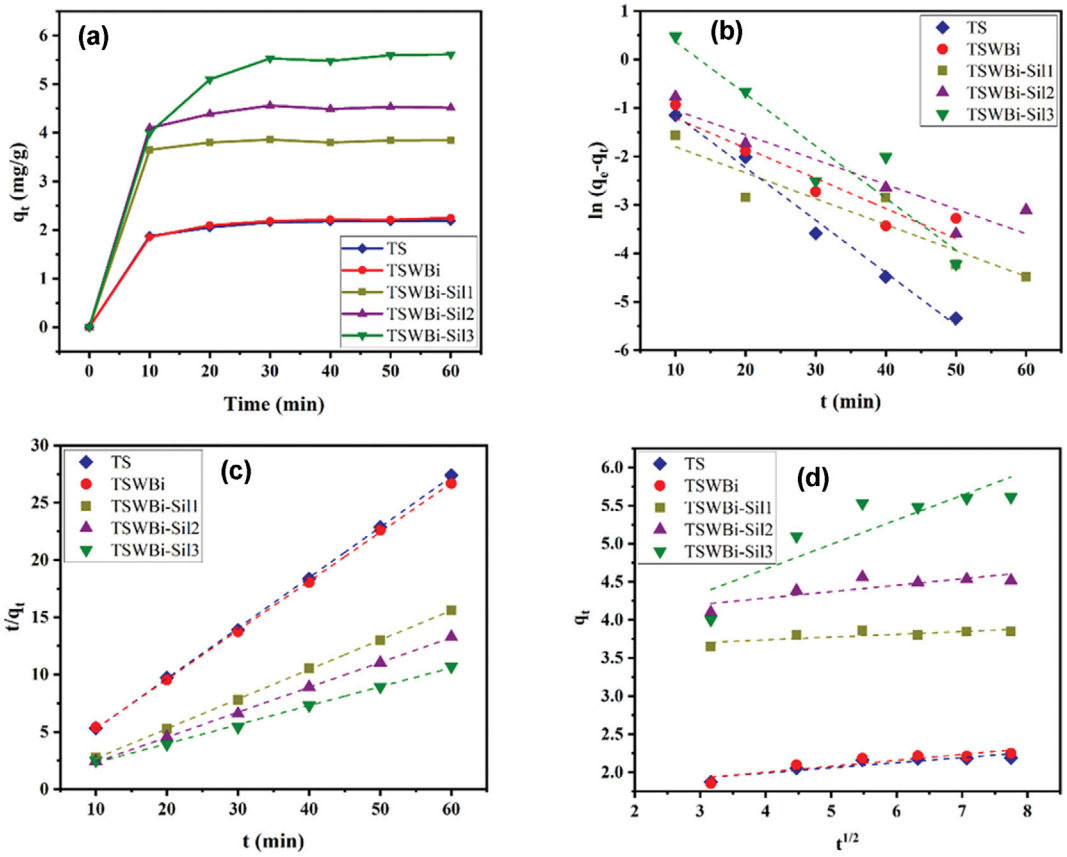

Fig. 15. (a) Influence of contact time on the adsorption capacity of RhB onto the synthesized samples; and the experimental data for the adsorption of RhB onto different photocatalyst-adsorbents at dark condition fitted to (b) pseudo-first order, (c) pseudo-second order, and (d) intra-particle diffusion models.

which can postpone the formation of ester bond among the surface hydroxyl group and the carboxylic group of RhB. Therefore, the silylation of TSWBi avoids an interaction between the carboxylic group of dye and the photocatalyst surface. In addition, the adsorption of RhB on the silylated photocatalysts increased with the loading of HMDS following the order TSWBi-Sil3 (56%)> TSWBi-Sil2 (45%)>TSWBi-Sil1 (38%), respectively. Thus, as shown in Fig. 15(a), the equilibrium adsorption capacity of all silylated photocatalysts is remarkably higher than TS and TSWBi, confirming the effect of silylation on the adsorption of RhB in the dark condition. This can be ascribed to replacing more surface hydroxyl groups with the more hydrophobic silyl groups at higher HMDS loading, leading to increased surface hydrophobicity and dye adsorption. This may facilitate diffusion of the bulky RhB molecules into the SiO_2 mesopores, where most active W- and Bi-promoted TiO_2 sites are located. Consequently, the removal of RhB on the silylated samples was accelerated due to the increased adsorption capacity and selectivity for dye and subsequent photocatalytic degradation [57]. Note that the photocatalytic activity of silylated samples showed an opposite trend with the BET surface area, indicating a non-correlation between them. Thus, the improvement of total photoactivity of silylated TSWBi was mainly caused by the increased surface hydrophobicity. To further explore the adsorption mechanism, three well-known kinetics models, pseudo-first-order (Eq. (1)), pseudo-second-order (Eq. (2)), and intra-particle diffusion (Eq. (3)), were evaluated.

$$\ln(q_e - q_t) = \ln(q_e) - k_1 t \quad (1)$$

$$\frac{t}{q_t} = \frac{1}{k_2 q_e^2} + \frac{t}{q_e} \quad (2)$$

$$q_t = k_{id} t^{1/2} + C \quad (3)$$

where q_e and q_t (mg g^{-1}) are adsorption capacities at equilibrium and time t, k_1 (min^{-1}) is the rate constant of the pseudo-first-order kinetic model, k_2 (g mg^{-1} min^{-1}) is the rate constant of pseudo-second-order kinetic model, and k_{id} (mg g^{-1} $min^{-0.5}$) represents the rate constant of the intra-particle diffusion kinetic model [58,59]. Table 2 and Fig. 15(b)-(d) exhibit linear fitting data related to the adsorption of RhB onto the photocatalyst-adsorbents before the visible light degradation. It is obvious from the linear plots fitted to the data and the correlation coefficients (R^2) that the pseudo-second-order model best matched the adsorption of RhB onto all of the prepared photocatalyst-adsorbents, which proposes the chemisorption is the rate-determining step during the adsorption process.

Accordingly, the effective diffusion of dye molecules through photocatalyst mesopores leads to the enhanced photocatalytic deg-

Table 2. Kinetics parameters for the adsorption of RhB onto different photocatalyst-adsorbents

Sample	R^2			q_e (mg g^{-1})	K_2 (g mg^{-1} min^{-1})
	Pseudo-first-order	Pseudo-second-order	Intra-particle diffusion		
TS	0.9874	0.9998	0.8220	2.2693	0.2319
TSWBi	0.8943	0.9998	0.8282	2.3330	0.1837
TSWBi-Sil1	0.8010	0.9999	0.6325	3.8774	0.5315
TSWBi-Sil2	0.8795	0.9997	0.6865	4.6074	0.2307
TSWBi-Sil3	0.8962	0.9982	07650	6.0495	0.0404

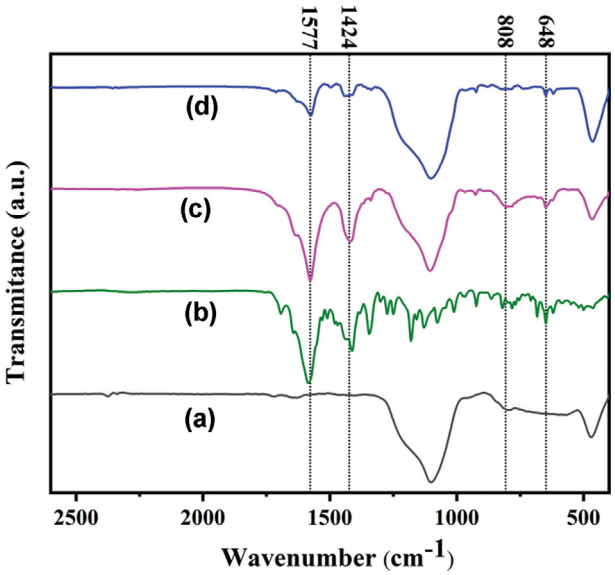

Fig. 16. FTIR spectra of (a) TSWBi-Sil3, (b) RhB, (c) TSWBi-Sil3 after adsorption of RhB, and (d) TSWBi-Sil3 after photodegradation of RhB.

radation of dye. The diffusion process can significantly enhance the interaction among the active sites and RhB molecules and improve the preferential adsorption of dye on SiO_2 substrate in the presence of H_2O molecules. Meanwhile, The RhB molecules were attacked by photo-generated electron-hole pairs, which implies that the silylated materials act as a photocatalyst beside the adsorbent. Subsequently, the resulting by-products seep into the solution through the pores. TSWBi-Sil3, after the adsorption and photodegradation of RhB, as well as the pure RhB dye, were probed by FTIR to gain a deeper understanding of the mechanism of the RhB degradation, as indicated in Fig. 16. As clearly seen, after adsorption, the characteristic peaks were detected at 648, 808, 1,424, and 1,577 cm^{-1}. The strong peak centered at 1,577 cm^{-1} is ascribed to the C=N stretching vibration, whereas the peak at 1,424 cm^{-1} is ascribed to the whole ring stretching vibration, and also, the peaks at 808 and 648 cm^{-1} correspond to the aromatic sp^2 C-H bending vibration [60], which confirms the adsorption of RhB on the photocatalyst surface during the dark condition. But further loading of the silyl groups beyond the optimal value caused excessive hydrophobicity of the surface, leading to poor dispersion of photocatalyst in aqueous media. All photocatalysts thoroughly degraded RhB after 3 h under visible light irradiation. Because of the slightly large band gap of anatase TiO_2 bandgap (~3.2 eV) [61], the photoactivity observed for TS sample can be attributed to the photosensitization process on this sample. In addition, the TS sample might be partially excited by UV light present in the irradiation spectrum of the tungsten halogen lamp [62]. The TSWBi presented higher visible light activity compared with TS sample, implying the effect of W and Bi on the improvement of visible-light response of composite. As shown in Fig. 16, the strength of all detected peaks ascribed to the RhB decreased significantly after photodegradation, which indicates the degradation of dye is relatively complete. Of note is that after TSWBi-Sil3 photocatalytic reaction, there is no effect of RhB in the solution or the photocatalyst surface, and these small peaks are probably ascribed to the by-products.

According to the correlation between the adsorption capacity of photocatalyst and its photoactivity, it can be concluded that silyl groups on the surface only act as adsorption sites under visible light. As a result, the W and Bi oxides species are responsible for the enhanced photocatalytic performance of samples prepared in this work.

CONCLUSIONS

Nanostructured mesoporous W- and Bi-promoted TiO_2/SiO_2 mixed oxides were prepared using wet impregnation method, and then different surface-silylated materials were prepared via a silylation process using different loadings of HMDS as the silylating reagent. The results show that the physicochemical trait and photocatalytic-adsorptive behavior of the as-prepared nanocomposites were significantly affected by SiO_2 support, W and Bi promoters, and surface silylation. The photoactivity under the visible light irradiation was enhanced by the W and Bi oxide species with a low loading of only 1.0 wt%. The increased surface hydrophobicity can be attributed to the replacement of surface hydroxyl groups with silyl groups, leading to greater adsorption of RhB molecules on the silylated surfaces. The optimized silylated photocatalyst (TSWBi-Sil3) exhibited the best performance, which could remove ~100% of RhB in less than 60 min. This can be ascribed to the synergistic impact of mesoporous texture, promoters, and improved hydrophobicity, leading to the simultaneous adsorptive and photocatalytic roles.

ACKNOWLEDGEMENTS

This research did not receive any specific grant from funding agencies in the public, commercial, or not-for-profit sectors.

REFERENCES

1. H. Zangeneh, A. A. L. Zinatizadeh, M. Habibi, M. Akia and M. H. Isa, *J. Ind. Eng. Chem.*, **26**, 1 (2015).
2. P. A. K. Reddy, P. V. L. Reddy, E. Kwon, K.-H. Kim, T. Akter and S. Kalagara, *Environ. Int.*, **91**, 94 (2016).
3. J. Shi, W. Huang, H. Zhu, J. Xiong, H. Bei, X. Wei and S. Wang, *Mater. Lett.*, **279**, 128472 (2020).
4. A. Salama, A. Mohamed, N. M. Aboamera, T. A. Osman and A. Khattab, *Appl. Nanosci.*, **8**, 155 (2018).
5. S. Feizpoor, A. Habibi-Yangjeh, K. Yubuta and S. Vadivel, *Mater. Chem. Phys.*, **224**, 10 (2019).
6. H. Anwer, A. Mahmood, J. Lee, K.-H. Kim, J.-W. Park and A. C. K. Yip, *Nano Res.*, **12**, 955 (2019).
7. Y.-H. Chiu, T.-F. M. Chang, C.-Y. Chen, M. Sone and Y.-J. Hsu, *Catalysts*, **9**, 430 (2019).
8. Y. Yu, M. Zhu, W. Liang, S. Rhodes and J. Fang, *RSC Adv.*, **5**, 72437 (2015).
9. M. A. Rauf and S. S. Ashraf, *Chem. Eng. J.*, **151**, 10 (2009).
10. X. Sun, L. Yan, R. Xu, M. Xu and Y. Zhu, *Colloids Surf. A Physicochem. Eng. Asp.*, **570**, 199 (2019).
11. L. A. Calzada, R. Castellanos, L. A. García and T. E. Klimova, *Micropor. Mesopor. Mater.*, **285**, 247 (2019).
12. M.-C. Roşu, C. Socaci, V. Floare-Avram, G. Borodi, F. Pogăcean, M. Coroş, L. Măgeruşan and S. Pruneanu, *Mater. Chem. Phys.*, **179**, 232 (2016).
13. M. Al Ruqaishy, F. Al Marzouqi, K. Qi, S. Liu, S. Karthikeyan, Y. Kim, S. M. Z. Al-Kindy, A. T. Kuvarega and R. Selvaraj, *Korean J. Chem. Eng.*, **35**, 2283 (2018).
14. D. Kwon and J. Kim, *Korean J. Chem. Eng.*, **37**, 1226 (2020).
15. R. Ameta, S. Benjamin, A. Ameta and S. C. Ameta, *Mater. Sci. Forum*, **734**, 247 (2012).
16. S. M. Patil, S. P. Deshmukh, K. V More, V. B. Shevale, S. B. Mullani, A. G. Dhodamani and S. D. Delekar, *Mater. Chem. Phys.*, **225**, 247 (2019).
17. R. Dewil, D. Mantzavinos, I. Poulios and M. A. Rodrigo, *J. Environ. Manage.*, **195**, 93 (2017).
18. M. R. D. Khaki, M. S. Shafeeyan, A. A. A. Raman and W. M. A. W. Daud, *J. Environ. Manage.*, **198**, 78 (2017).
19. M. Scarisoreanu, A. G. Ilie, E. Goncearenco, A. M. Banici, I. P. Morjan, E. Dutu, E. Tanasa, I. Fort, M. Stan, C. N. Mihailescu and C. Fleaca, *Appl. Surf. Sci.*, **509**, 145217 (2020).
20. M. Mousavi, M. Soleimani, M. Hamzehloo, A. Badiei and J. B. Ghasemi, *Mater. Chem. Phys.*, **258**, 123912 (2021).
21. M. M. Mahlambi, C. J. Ngila and B. B. Mamba, *J. Nanomater.*, **2015**, 1 (2015).
22. M. R. Al-Mamun, S. Kader, M. S. Islam and M. Z. H. Khan, *J. Environ. Chem. Eng.*, **7**, 103248 (2019).
23. H. Dong, G. Zeng, L. Tang, C. Fan, C. Zhang, X. He and Y. He, *Water Res.*, **79**, 128 (2015).
24. D. Chen, Y. Cheng, N. Zhou, P. Chen, Y. Wang, K. Li, S. Huo, P. Cheng, P. Peng, R. Zhang, L. Wang, H. Liu, Y. Liu and R. Ruan, *J. Clean. Prod.*, **268**, 121725 (2020).
25. G. Zhang, A. Song, Y. Duan and S. Zheng, *Micropor. Mesopor. Mater.*, **255**, 61 (2018).
26. M. Chang, H. Hu, Y. Zhang, D. Chen, L. Wu and X. Li, *Nanomaterials*, **7**, 104 (2017).
27. J. Chen, S. Qin, Y. Liu, F. Xin and X. Yin, *Res. Chem. Intermed.*, **40**, 637 (2014).
28. D. Xu, Y. Hai, X. Zhang, S. Zhang and R. He, *Appl. Surf. Sci.*, **400**, 530 (2017).
29. M. Malligavathy, S. Iyyapushpam, S. T. Nishanthi and D. P. Padiyan, *J. Mater. Sci. Mater. Electron.*, **28**, 18307 (2017).
30. Q. Peng, G. Peng, L. Wu, X. Wang, X. Yang and X. Li, *Res. Chem. Intermed.*, **44**, 6753 (2018).
31. E. Mugunthan, M. B. Saidutta and P. E. Jagadeeshbabu, *Environ. Nanotechnol., Monit. Manag.*, **10**, 322 (2018).
32. M. B. Tahir, M. Sagir and K. Shahzad, *J. Hazard. Mater.*, **363**, 205 (2019).
33. P. Haghighi, S. Alijani, A. Bazyari and L. T. Thompson, *J. Photochem. Photobiol. A Chem.*, **426**, 113790 (2022).
34. H. Liu, D. Yu, T. Sun, H. Du, W. Jiang, Y. Muhammad and L. Huang, *Appl. Surf. Sci.*, **473**, 855 (2019).
35. C. Gomez-Polo, S. Larumbe, A. Gil, D. Muñoz, L. R. Fernández, L. F. Barquín, A. García-Prieto, M. L. Fdez-Gubieda and A. Muela, *Surf. Interfaces*, **22**, 100867 (2021).
36. M. Kassir, T. Roques-Carmes, T. Hamieh, J. Toufaily, M. Akil, O. Barres and F. Villiéras, *Colloids Surf. A Physicochem. Eng. Asp.*, **485**, 73 (2015).
37. M. Yan, G. Zeng, X. Li, C. Zhao, G. Yang, J. Gong, G. Chen, L. Tang and D. Huang, *New J. Chem.*, **41**, 4377 (2017).
38. Y. Kuwahara, K. Maki, Y. Matsumura, T. Kamegawa, K. Mori and H. Yamashita, *J. Phys. Chem. C*, **113**, 1552 (2009).
39. Y. Kuwahara, T. Kamegawa, K. Mori, Y. Matsumura and H. Yamashita, *Top. Catal.*, **52**, 643 (2009).
40. K. Guesh, Á. Mayoral, C. Marquez-Alvarez, Y. Chebude and I. Diaz, *Micropor. Mesopor. Mater.*, **225**, 88 (2016).
41. N. N. Bahrudin and M. A. Nawi, *Korean J. Chem. Eng.*, **36**, 478 (2019).
42. M. Baruah, S. L. Ezung, A. Supong, P. C. Bhomick, S. Kumar and D. Sinha, *Korean J. Chem. Eng.*, **38**, 1277 (2021).
43. Y. Kuwahara, T. Kamegawa, K. Mori and H. Yamashita, *Chem. Commun.*, **39**, 4783 (2008).
44. T. Ohno, T. Tsubota, K. Kakiuchi, S. Miyayama and K. Sayama, *J. Mol. Catal. A Chem.*, **245**, 47 (2006).
45. N. L. Reddy, S. Emin, M. Valant and M. V Shankar, *Int. J. Hydrogen Energy*, **42**, 6627 (2017).
46. Y. Yamin, N. Keller and V. Keller, *J. Photochem. Photobiol. A Chem.*, **245**, 43 (2012).
47. A. R. Almeida, J. T. Carneiro, J. A. Moulijn and G. Mul, *J. Catal.*, **273**, 116 (2010).
48. G. Zhang, J. Yi, J. Shim, J. Lee and W. Choi, *Appl. Catal. B Environ.*, **102**, 132 (2011).
49. L. Li, X. Wang, D. Zhang, R. Guo and X. Du, *Appl. Surf. Sci.*, **328**, 26 (2015).
50. U. Mahanta, M. Khandelwal and A. S. Deshpande, *Appl. Surf. Sci.*, **576**, 151745 (2022).
51. Q. Jiang, J. Huang, B. Ma, Z. Yang, T. Zhang and X. Wang, *Colloids Surf. A Physicochem. Eng. Asp.*, **602**, 125112 (2020).
52. E. Pakdel, W. A. Daoud, S. Seyedin, J. Wang, J. M. Razal, L. Sun and X. Wang, *Colloids Surf. A Physicochem. Eng. Asp.*, **552**, 130 (2018).
53. D. R. Eddy, S. N. Ishmah, M. D. Permana and M. L. Firdaus, *Cata-*

lysts, **10**, 1248 (2020).
54. Q. Qin and Y. Xu, *Micropor. Mesopor. Mater.*, **232**, 143 (2016).
55. N. Lv, Y. Li, Z. Huang, T. Li, S. Ye, D. D. Dionysiou and X. Song, *Appl. Catal. B Environ.*, **246**, 303 (2019).
56. M. Xing, D. Qi, J. Zhang, F. Chen, B. Tian, S. Bagwas and M. Anpo, *J. Catal.*, **294**, 37 (2012).
57. H. Yamashita and H. Li, *Nanostructured Photocatalysts*, Springer (2016).
58. B. Shojaei, R. Miri, A. Bazyari and L. T. Thompson, *Fuel*, **321**, 124136 (2022).
59. K. Mirzaei, E. Jafarpour, A. Shojaei and H. Molavi, *Ind. & Eng. Chem. Res.*, **61**, 11735 (2022).
60. V. A. Tran, K. B. Vu, T.-T. T. Vo, H. H. Do, L. G. Bach and S.-W. Lee, *Appl. Surf. Sci.*, **538**, 148065 (2021).
61. D. Li, N. Ohashi, S. Hishita, T. Kolodiazhnyi and H. Haneda, *J. Solid State Chem.*, **178**, 3293 (2005).
62. J. Zhao, T. Wu, K. Wu, K. Oikawa, H. Hidaka and N. Serpone, *Environ. Sci. Technol.*, **32**, 2394 (1998).